Low Pd loadings onto Printex L6: synthesis, characterization and performance towards H_2O_2 generation for electrochemical water treatment technologies

Guilherme V. Fortunato[a, 1, *], Matheus S. Kronka[a, 1], Alexsandro J. dos Santos[a, 1, *], Marc Ledendecker[b], and Marcos R.V. Lanza[a, *]

[a] Institute of Chemistry of São Carlos, University of São Paulo, Avenida Trabalhador São-Carlense 400, São Carlos, SP 13566-590, Brazil

[b] Department of Technical Chemistry, Technical University Darmstadt, Alarich-Weiss-Straße 8, 64287 Darmstadt, Germany

[1] These authors contributed equally to this work.

*Corresponding author's e-mails:
g.fortunato@usp.br (G.V. Fortunato)
alexsandrojhones@usp.br (A.J. dos Santos)
marcoslanza@usp.br (M.R.V. Lanza)

Abstract

In order to enhance hydrogen peroxide (H_2O_2) electrogeneration a catalyst based on less than 1 wt.% of Pd nanoparticles dispersed onto commercially available Printex L6 carbon black (PCL6) is proposed and synthetized. The material was characterized by physico-chemical and electroanalytical methods, demonstrating high activity with a 320 mV lower onset potential compared to pristine PCL6 and high stability after 5,000 potential cycles. Its performance places it among the most efficient bi- and monometallic electrocatalysts for H_2O_2 production. When testing the accumulation of H_2O_2, a 1.69-fold molar increase was observed for $Pd_{1\%}$/PCL6 compared to PCL6. Different electrochemical advanced oxidation processes based on H_2O_2 generation have been performed to oxidize and remove pollutants as exemplarily shown on methyl paraben in Na_2SO_4 solution as model pollutant. A boron-doped diamond electrode was used as anode while $Pd_{1\%}$/PCL6 was tested in a rotating ring disk electrode (RRDE) and gas diffusion setup. Pollutant degradation followed a pseudo-first-order reaction kinetic in the following order: anodic oxidation along with H_2O_2 generation (AO-H_2O_2) < AO-H_2O_2/UVC < electro-Fenton (EF) < photoelectro-Fenton (PEF). The best mineralization performance was found for PEF due to the photodecarboxylation of Fe (III) complexes with UVC light, while the process with lowest energy consumption per order was EF with 0.488 kWh m^{-3} $order^{-1}$. At the end of the work a route for pollutant mineralization was suggested.

Keywords: H_2O_2 electrogeneration, palladium, wastewater treatment, electrochemical advanced oxidation processes, methyl paraben

1. Introduction

Hydrogen peroxide (H_2O_2) plays a critical role in a wide range of industrial, commercial, and domestic applications, including wastewater treatment (Campos-Martin et al., 2006; Pesterfield, 2009; Edwards et al., 2015; Jiang et al., 2018). Technologies based on the *in-situ* electrochemical H_2O_2 production via the oxygen reduction reaction (ORR, Eq. (1)) represent an environmentally friendly way to generate H_2O_2 overcoming its transportation and storage drawbacks (Carneiro et al., 2017).

$$O_2 + 2H^+ + 2e^- \rightarrow H_2O_2 \qquad (1)$$

Electrochemical advanced oxidation processes (EAOP) based on H_2O_2 such as anodic oxidation with H_2O_2, (AO-H_2O_2), electro-Fenton (EF) and photoelectro-Fenton (PEF) allow the generation of reactive oxygen species such as hydroxyl radicals (•OH) (Brillas, 2020; Moreira et al., 2017). This strong oxidizing agent (E^o(•OH/H_2O) = 2.80 V_{SHE}) is capable of non-selectively convert organic pollutants to less toxic products or even total mineralization to carbon dioxide, water and inorganic ions (dos Santos et al., 2018a). In the last decade, the H_2O_2-EAOPs have been widely used in the treatment of dyes (Brillas and Martínez-Huitle, 2015; dos Santos et al., 2020, 2016; Nakamura et al., 2019; Paz et al., 2018), pesticides (Carneiro et al., 2018; Dominguez et al., 2018; Rosa Barbosa et al., 2018; Fdez-Sanromán et al., 2020), and pharmaceutics (Dirany et al., 2012; Ganiyu et al., 2016; Zhang et al., 2019; Lima et al., 2020) in synthetic and real effluents (dos Santos et al., 2018a; Ganiyu et al., 2018; Ren et al., 2020). However, an obstacle being faced in the electrochemical production of H_2O_2 and its coupling to EAOPs is the development of efficient catalyst materials that selectively reduce O_2 to H_2O_2 (Fellinger et al., 2012; Siahrostami et al., 2013; Verdaguer-casadevall et al., 2014). Active and selective ORR (electro)catalysts to form H_2O_2 must have sufficiently strong interaction with O_2 so that the reaction can occur on the catalysts surface without breaking the intermolecular O=O bond (Lobyntseva et al., 2007;Fellinger et al., 2012; Siahrostami et al., 2013; Choi et al., 2014; Verdaguer-casadevall et al., 2014). An ideal catalyst should demonstrate high selectivity, activity and stability at low costs. Recent studies demonstrated that the metal loading in the carrier material affect the activity and selectivity toward ORR (Inaba et al., 2004; Schneider et al., 2008; Nesselberger et al., 2013; Fabbri et al., 2014; Taylor et al., 2016; Fortunato et al., 2018). At low metal loading, the selectivity for H_2O_2 increases and the O-O bond breakage is suppressed. As an example, the group of Arenz (Nesselberger et al., 2013) evaluated the effect of Pt-particle proximity on the catalytic ORR activity. They noticed a decrease in ORR activity with increase of the inter particle distance (*ipd)*. The diffusion-limited current decreased at lower cluster density (increasing *ipd*), suggesting a shift of the ORR mechanism from 4e$^-$ to 2e$^-$. Fabbri and co-workers (Fabbri et al., 2014) supported different Pt loadings onto carbon and realized that the transition from dispersed Pt nanoparticles to extended surfaces strongly influences ORR selectivity. Highly dispersed nanoparticles promote significantly the production of H_2O_2.

Effects on selectivity caused by varied catalyst loading and *ipd* were also suggested for Pd (Fortunato et al., 2018; Mittermeier et al., 2017). Catalysts with different Pd loadings and different *ipd* onto different carbon supports have been synthesized and tested (Fortunato et al., 2018). Low Pd-catalyst loadings (<2 wt%) and high *ipd* (>125 nm) achieve selectivities to H_2O_2 close to 100% at low overpotentials resulting in high mass activities. The strong interaction between carbonaceous materials and metal nanoparticles (catalyst-support interaction), which may be responsible for changes of metal cluster electronic properties, becomes a key contributor to achieve the observed catalytic performance as well as the long-term stability (Fortunato et al., 2018; Ma et al., 2013). Carbon materials such as graphene and carbon black have been reported to be selective towards H_2O_2 in alkaline (Assumpção et al., 2011; Wu et al., 2017; Han et al., 2019; Jiang et al., 2019; Kim et al., 2019; Cordeiro-Junior et al., 2020) and acidic (Fellinger et al., 2012; Zhang et al., 2018; Kim et al., 2019; Melchionna et al., 2019) medium, mainly due to their oxygenated and nitrogenated functional groups. However, in acidic conditions, the ORR typically takes place at high overpotentials (Cordeiro-Junior et al., 2020; Daems et al., 2014; Fellinger et al., 2012; Lu et al., 2019). Additionally, oxygenated and nitrogenated functional groups in carbon materials offer ample anchor sites to stabilize metal catalysts.(Antolini, 2012; Barros et al., 2015; Fortunato et al., 2016, 2018; Luo and Alonso-Vante, 2015; Ma et al., 2013).

In this work, a highly active, selective and stable catalyst toward the production of H_2O_2 is synthetized and evaluated using less than 1 wt.% of Pd nanoparticles (NPs) well dispersed onto commercially available Printex L6 carbon black (PCL6), a carbonaceous material with oxygenated and nitrogenated functional groups (Assumpção et al., 2011). The $Pd_{1\%}$/PCL6 catalyst was analyzed by physical characterization techniques and electroanalytical methods. Besides the significantly enhanced activity/selectivity/stability compared to commonly applied carbon black and Pd-based materials, the novelty of the here described study lies in the fact of the *in-situ* produced H_2O_2 in a gas diffusion electrode (GDE) setup was evaluated and used to catalyze the degradation of methyl paraben (MetP), chosen as exemplary organic pollutant. MetP is a well-known endocrine disruptor with potential harmful effects to environment and human life when incorrectly disposed (Dionisio et al., 2020; Gmurek et al., 2015; Steter et al., 2016). The performance of the catalyst in the electrogeneration of H_2O_2 was evaluated galvanostatically, following the pollutant concentration, its mineralization and formed by-products and a degradation was route suggested. The energy consumption per order was determined as well.

2. Experimental section

2.1 Reagents

MetP with 99% purity was acquired from Supelco. The salts and precursor solutions employed were palladium chloride ($PdCl_2$), sulfuric acid (H_2SO_4), potassium sulfate (K_2SO_4), sodium sulfate (Na_2SO_4), ascorbic acid (AA) and dimethylformamide ($(CH_3)_2NC(O)H$), all acquired from Vetec. Sodium sulfate (Na_2SO_4) and Iron (II) sulfate heptahydrate ($FeSO_4·7H_2O$) were of analytical grade and supplied by Sigma-Aldrich. All solutions were prepared with ultrapure water obtained from a Milli-Q system with resistivity >18 MΩ cm at 25ºC. All other chemicals used for analysis were of analytical grade or HPLC grade provided by Sigma-Aldrich.

2.2 Synthesis of $Pd_{1\%}$/PCL6

Firstly, the Printex carbon (PCL6, from Evonik®) was thermally treated at 120 °C for 24 h. $Pd_{1\%}$/PCL6 electrodes were synthesized by the hydrothermal procedure proposed in (Fortunato et al., 2018). Briefly, 160 mg of PCL6 were dispersed with 3 mg of $PdCl_2$ in 20 mL of ultrapure water under ultra-sonication bath for 1 h. Afterwards, the mixture was heated up to its boiling point using a hot plate with magnetic stirring. Subsequently, 78 mg of AA (previously solubilized in 2 mL of water) were added. After 5 minutes, the heating was stopped and the mixture was kept stirring for 2 hours. The formed nanocomposite was washed 15 times by centrifugation to remove the unreacted species present in the mixture, and finally dried in an oven at 60 °C overnight. In order to have a gas diffusion electrode (GDE) to perform EAOPs, a carbon cloth (PW03 - 33" wide, 80 yards long - average 15.6 pounds per roll, acquired from Plain Weave Fabric) with geometric area of 2.7 cm^2 was used as substrate to the deposition of the produced film of 200 $\mu g\ cm^{-2}$ by dropping

206 mL of 2.5 mg mL^{-1} catalyst solution and addition of 100 µL of a Nafion 0.1% on isopropanol solution. Afterwards, it was dried under N_2-gas flow for 2 h in an open system.

2.3 Physico-chemical characterization methods

To perform transmission electron microscopy (TEM) and scanning-TEM (STEM) experiments, the catalyst dispersion was drop-casted onto a TEM grid constituted by a lacey carbon film on a copper grid (300-mesh acquired from Electron Microscopy Sciences). TEM and STEM analyses were conducted using a FEI TECNAI G² F20 HRTEM microscope at 200 kV. For the determination of Pd loading, a TGA-50 thermogravimetric analyzer (Shimadzu) was used; samples of 2–5 mg were placed under a synthetic air 5.0 FID gas flow (50 mL min^{-1}) at temperatures ranging between 25-900 °C, at a heating rate of 10 °C min^{-1}, using alumina crucibles. The X-ray photoelectron spectroscopy (XPS) analyses were performed using a Scienta Omicron ESCA+ spectrometer.

The Al Kα line (energy =1486.6 eV) was used as excitation source operating at 20 kV and 25 W. The binding energies were calibrated using the C1s signal (284.6 eV) as reference. The Shirley method was used to subtract the inelastic noise from the narrow scan (High-resolution) spectra. The composition (at. % and mass conc. %) of the surface (<5 nm) was estimated by using the (relative) peak area proportions compensated by Scofield atomic sensitivity factors (accuracy of ± 5%) (Scofield, 1976) from the narrow scan spectra. For the Pd 3d region spectrum, deconvolution, a Voigt type function with Gaussian and Lorentzian (in a proportion of 70:30) combinations was used. Structural characterization was carried out based on X-ray diffraction (XRD) measurements. The XRD measurements were performed with the aid of a Bruker X-ray diffractometer model D8 Advance, operating at 40 kV and 40 mA (1.6 kW), using Cu-Kα radiation

(λ = 1.540501 Å / 8,047keV). The scan rate applied was 0.02° s^{-1} in 2θ, and silicon powder was employed as reference.

2.4 Treatment of MetP by EAOPs

Assays were performed in a bench scale electrochemical cell with an external jacket for thermostatic water recirculation at 25 °C (dos Santos et al., 2016). Pure O_2 was coupled to the GDE to ensure the fed of oxygen gas at 500 mL min^{-1} in order to electrogenerate H_2O_2 from Eq. (1). A boron-doped diamond (BDD) thin film with a geometric area of 3.0 cm^2 was used as anode. The interelectrode gap was kept around 1.0 cm. Before each experiment, both anode and cathode were activated by using a 50 mM $NaSO_4$ at pH 2.5 and j = 100 mA cm^{-2} during 60 min (dos Santos et al., 2019).

Electrolysis at constant current density (*j*) at 33.3 mA cm^{-2} was performed at an Instrutherm DC power supply FA-2030 coupled to Instrutemp ITMDB 100 ampere meter and Instrutemp MDB-450 voltmeter. All experiments were carried out with 150 mL of 0.50 mM MetP solution with 50 mM Na_2SO_4 as support electrolyte. Before electrolysis, the solution pH was adjusted to 2.5 using a pH-meter ION pHB500 with a diluted H_2SO_4 solution. Acidic conditions are considered the best for Fenton's reactions, since it avoids the precipitation of iron. All the processes were performed under pH 2.5, in order to maintain the same operating conditions for comparison between the different EAOPs.

Different concentrations Fe^{2+} (0.1, 0.25 and 0.50 mM) were tested to perform EF and PEF treatment. In PEF, the solution was illuminated with a 5W UVC lamp (Pen-Ray model 11SC-2.12) that provided 19 Wm^{-2} of irradiance.

2.5 Analytical techniques

The H_2O_2 concentration was determined by the Molybdate method where the absorbance of the colored complex formed with H_2O_2 and $(NH_4)_6Mo_7O_{24}$ was measured at λ = 350 nm using a Shimadzu UV-1900 spectrophotometer (Lima et al., 2020). This value allowed the calculation of the percentage of current efficiency (CE) following Faraday's law (Eq. (2)):

$$CE_{\mathrm{H_2O_2}}(\%) = \frac{2\ \mathrm{F}\ \mathrm{C_{H_2O_2}} \mathrm{V_s}}{I\ t} \times 100 \qquad (2)$$

Where 2 corresponds to the number of electrons needed to the reduction of O_2 to form H_2O_2, F to the Faraday constant (96,487 C mol^{-1}), $\mathrm{C_{H_2O_2}}$ to the H_2O_2 concentration in mol L^{-1}, V_s to the volume of the solution in L, I to the applied current intensity in A, and t to the reaction time in s.

The concentration of MetP was determined on a high-performance liquid chromatography (HPLC) system equipped with a Phenomenex Luna C18 (250 x 4.6 mm, 5μm) column and a Supelcosil C18 (4 mm x 3.0 mm i.d.) pre-column at 35 ºC and coupled to an SPD-20A UV detector selected at λ = 258 nm. The mobile phase consisted of an aqueous solution containing water-acetonitrile mixture (60/40, v/v) at a flow rate of 1.0 mL min^{-1}. The retention time for MetP was 6.3 min. The acid intermediates were analyzed by ion exchange chromatography. The ion exchange column used was Metrosep Organic Acids (250 mm/7.8 mm) from Metrohm, whereas a diluted H_2SO_4 solution (5 mmol L^{-1}) was employed as the solvent in 20 μL sample injection and 20 min of running. Analyzes were performed on an 850 Profissional IC ion chromatograph (Metrohm) using a conductivity detector. Total organic carbon (TOC) was obtained using a Shimadzu TOC-VCPN equipment and its removal is given by Eq. (3). All withdrawn samples before HPLC and TOC analyzes were filtered with 0.45 μm filters (chromafil Xtra PET-45/25).

The experiments were carried out in duplicate and figures related to degradation and mineralization show the error bar related to the 95% confidence interval.

$$TOC\ removal\ (\%) = \frac{TOC_0 - TOC_f}{TOC_0} \times 100 \qquad (3)$$

The percentage of mineralization current efficiency (MCE) was calculated from Eq. (4):

$$MCE\ (\%) = \frac{nFV\Delta(TOC)_{exp}}{4.32\times10^7\ m\ I\ t} \times 100 \qquad (4)$$

Where 4.32×10^7 is the conversion factor (3,600 s h^{-1} × 12,000 mg C mol^{-1}), m is the number of carbon atoms of MetP molecule (m = 8). The number of electrons (n) for the mineralization process was taken as 34 considering the theoretical mineralization for the MetP (Steter et al., 2016) (Eq. (5)):

$$C_8H_8O_3 + 13\ H_2O \rightarrow 8\ CO_2 + 34\ H^+ + 34\ e^- \qquad (5)$$

In order to follow the evolution of by-products of MetP degradation by gas chromatography–mass spectrometry (GC-MS), the samples were extracted in C_2Cl_2 using a flow of 1 mL of $N_{2(g)}$ to concentrate the organic compounds for analyses. This analysis was executed in a gas chromatograph GC-2010 Plus coupled to a mass spectrometer QP2020 (Shimadzu), equipped with an automatic sampler model AOC-6000. The column used was a non-polar capillary Rtx-5MS (30 m × 0.25 mm × 0.25 µm) (Shimadzu) and Helium (purity 99.999%) was the carrier gas applied at a flow rate of 1.0 mL min^{-1}. The initial temperature of the oven was 36 °C for 1 min, increased to 320 °C at 5 °C min^{-1}, hold for 10 min, totaling 67.80 min of analysis. There was a solvent cut time of 3 min. The injection volume was 1 µL of the liquid sample. The injection temperature was 250 °C and splitless injection was used. The mass spectrometer, equipped with an electron impact source (EI), was operated in SCAN mode at 70 eV of electronic energy. The ion source and interface temperatures were 230 and 280 °C, respectively.

3. Results and discussion

3.1 Physico-chemical characterization

Compared to metal-based materials, commercial PCL6 typically demonstrates relatively low activity toward ORR while the selectivity towards H_2O_2 both in alkaline (Assumpção et al., 2011; Barros et al., 2015) and acidic (Cordeiro-Junior et al., 2020) medium is rather high. Specifically at low pH values, the ORR takes place at high overpotentials emphasizing the need for better catalysts (Cordeiro-Junior et al., 2020; Lu et al., 2019). Its surface composition contains oxygen, sulfur, and nitrogen functional groups (Assumpção et al., 2011) that can assist to control the dispersion and the interaction with metallic species (metal-support interaction) (Antolini, 2012; Barros et al., 2015; Fortunato et al., 2016, 2018; Luo and Alonso-Vante, 2015; Ma et al., 2013). As aforementioned, Pd at low loadings (<2 wt%) and high *ipd* can achieve selectivities towards H_2O_2 close to 100% with low overpotentials (Fortunato et al., 2018). In this context, we combined these two effects (low metal loading and abundant carbon material with relatively high metal-support interaction) to produce an efficient catalyst toward H_2O_2 production via ORR. The challenge lies in distributing low amounts of Pd NPs homogeneously onto the carbon surface to obtain an *ipd* over 100 nm. The strategy proposed by Fortunato and co-authors (Fortunato et al., 2018) was used to tune the Pd loading so that high selectivities towards H_2O_2 can be achieved.

In Fig.s 1 and 2, the physico-chemical characterizations of the different catalysts are shown. For $Pd_{1\%}$/PCL6, a low Pd amount (~0.6 wt.%) resulted in highly dispersed Pd nanoparticles in the size range of ~5,5 nm with octahedral and spherical shapes and edge-to-edge interparticle distances around 170 nm, as shown in Fig. 1a-f (c.f. Table S1). The HR-TEM image (Fig. 1e) reveals lattice fringes of 0.22 nm (on average) which is expected for (1 1 1) face-centered cubic (*fcc*) planes of crystalline Pd (Fortunato et al., 2018; Saha et al., 2011; Venarusso et al., 2018; Vukmirovic et al., 2011). A metal loading of 0.9 wt.% was obtained by thermogravimetric analysis (c.f. Fig. 2a). The diffractograms (Fig. 2b) evidence the presence of less than 1 wt.% of Pd on PCL6 showing the patterns of *fcc* crystalline with peaks (1 1 1), (2 0 0), (2 2 0), (3 1 1), and less visible (2 2 2) for Pd (Boone and Maia, 2017; Kabir et al., 2016; Saha et al., 2011; Venarusso et al., 2018, 2016). The presence of a characteristic broad peak (0 0 2) at 2θ = 25.9°, associated to the graphitic structure of the carbon support (Boone and Maia, 2019, 2017; Kabir et al., 2016), is also observed. To resolve the surface characteristics, XPS measurements were performed. The XPS survey spectra (Fig. 2c) shows only peaks in the C 1s and O 1s regions due to the low Pd amount.

The narrow-scan spectrum in the Pd 3d region (Fig. 2d) exhibits the expected spin-orbit splitting and binding energy of metallic Pd species (Pd^0 $3d_{5/2}$ at ~335,4 eV, Pd^0 $3d_{3/2}$ at ~341,0 eV, c.f. Table S3), and as well as the spin-orbit splitting for oxidized Pd species (Pd^{2+} $3d_{5/2}$ at ~337,6 eV, Pd^{2+} $3d_{3/2}$ at ~343,0 eV, c.f. Table S3). The XPS analysis was not able to detect a signal in the Cl 2p region (Fig. S2), although we do not rule out the presence of Cl adsorbed to the Pd surface since halides can adsorb strongly to Pd surfaces enhancing H_2O_2 production. (Damjanovic et al., 1967; Marković et al., 1999; Schmidt et al., 2001; Su et al., 2018; Yan et al., 2011). High-resolution XPS quantification reveals ca. 0.10 at% Pd (=0.87 wt.%, c.f. Tables S1 and S2), which corresponds well to thermogravimetric analysis.

3.2 Electrochemical profile and ORR performance

Fig. 3 presents the CVs, RRDE, and RDE responses for PCL6 and $Pd_{1\%}$/PCL6. The CV obtained in N_2-saturated solution for the synthesized materials (Fig. 3a) reveals that in the absence of Pd, the characteristic quinone/hydroquinone peaks (at ~0.2 V) from the carbon surface (Fortunato et al., 2018; Jukk et al., 2013) are observed. Under O_2-saturated conditions, an additional peak at ~ -0.2 $V_{Ag/AgCl}$ was observed corresponding to the reduction of molecular oxygen. When ~1 wt.% Pd is present (c.f. Fig. 3b), in N_2-saturated solution, the characteristic polycrystalline Pd surface processes of hydrogen underpotential deposition (H_{UPD}) (-0.4 and 0 $V_{Ag/AgCl}$) are observed. Due the low metal loading (and presumable Cl-speciations on the surface), Pd oxidation in the potential region of 0.5-1.0 $V_{Ag/AgCl}$ is suppressed. Careful inspection of the corresponding oxide back reduction region (0.45-0.25 $V_{Ag/AgCl}$) reveals the expected oxide reduction peak at ~0.34 $V_{Ag/AgCl}$. Under O_2-saturated condition, with ~1 wt.% of Pd onto PCL6, the ORR peak appears at a potential ~500 mV more positive than the bare carbon matrix (c.f. Fig. 3a and 3b). For $Pd_{1\%}$/PCL6, a lower potential limit of -0.4 $V_{Ag/AgCl}$ was selected due the hydrogen production at lower potentials. Additionally, the electrochemically active surface area (*ECSA*) determined from the electrical double-layer capacitance revealed comparable surface areas for both catalysts. In the presence of Pd NPs, the *ECSA* decreases ~10% in comparison to pure PCL6 (78.4 *vs.* 86.5 $m^2\ g^{-1}{}_{catalyst}$, respectively —c.f. Table S4), which could be related to not fully covered glassy carbon areas.

Fig. 3c shows the linear sweep voltammetry in RRDE configuration. The samples were tested towards the production of H_2O_2 by scanning the potential from 0.1 to 1.0 $V_{Ag/AgCl}$ under O_2 saturation in 0.1 mol L^{-1} K_2SO_4 at pH 2.5. For pure PCL6, the onset potential for ORR occurs at ~ 0 $V_{Ag/AgCl}$. The disk current density achieves the diffusion-limited values at ~ -0.7 $V_{Ag/AgCl}$. The ring current densities are comparably large in comparison to the disk current densities, evidencing large H_2O_2 production amounts. From RRDE results, the potential dependent selectivity towards H_2O_2 (S_{H2O2}) in the course of the ORR could be obtained, and the responses are shown in Fig. 3d. The S_{H2O2} for PCL6 reaches ~ 84% over the measured potential range from -0.9 V to -0.15 $V_{Ag/AgCl}$, in line with previously reported results (Cordeiro-Junior et al., 2020). As stated before, Pd-loadings

>2 wt.% typically favor full reduction to H_2O. To test our hypothesis, PCL6 was modified with 20 wt.% Pd ($Pd_{20\%}$/PCL6) and tested towards the production of H_2O_2.

As expected, 20 wt.% of Pd leads to a drop in selectivity to ~10% over the measured potential range from -0.2 to 0.3 $V_{Ag/AgCl}$ (c.f. Fig. 3c and 3d). Additionally, one part of $Pd_{20\%}$/PCL6 was physically combined with 9 parts of PCL6. Here, the 2% Pd-loading leads to a drastic increase in H_2O_2 selectivity of over 80% (c.f. Fig. 3c and 3d).

Additionally, a set of LSV curves recorded at different rotation rates are presented in Fig. 3e and 3f. Below -0.6 $V_{Ag/AgCl}$ (Fig. 3e), the ORR is controlled by mass transport limitations for PCL6. For $Pd_{1\%}$/PCL6, the mass transport region is not well defined due the hydrogen evolution with occurs concomitantly below -0.2 $V_{Ag/AgCl}$. From these curves, the electron transfer number ($n_{K\text{-}L}$) at different potentials was estimated (see details in Support Information). PCL6 and $Pd_{1\%}$/PCL6 have average $n_{K\text{-}L}$ values of 1.9 and 2.9, respectively, supporting the high selectivity for 2-electron-transfer ORR on both catalysts. In order to evaluate the electrochemical stability performance for the catalyst surfaces, changes in the activity and selectivity were monitored by RRDE before and after 5,000 cycles between -0.2 and 0.5 $V_{Ag/AgCl}$ at a scan rate of 0.5 V s^{-1} and the results are presented in Fig. S4. In general, no drastic changes in electrocatalytic behavior, in terms of activity and selectivity, are observed for PCL6 and $Pd_{1\%}$/PCL6. The CVs prior to and after stability tests (c.f. Fig. S4b) show small differences in the electrochemical behavior, suggesting high stability of the carbon structures. Fig. S5c compares the electrocatalytic performance of $Pd_{1\%}$/PCL6 with other noble metal-based state-of-the-art catalysts reported in literature in terms of kinetic current densities to H_2O_2 as a function of applied potential. $Pd_{1\%}$/PCL6 shows high stability while maintaining high activity and selectivity relatively close to the most active Pd- and Pt-based catalysts. We point out that $Pd_{1\%}$/PCL6 is easily synthesized, demonstrate high reproducibility and can be produced on a large scale by using commercially available carbon black materials as well as omitting any toxic metal which would be detrimental in wastewater treatment devices.

3.3 MetP treatment by H_2O_2-based EAOPs

3.3.1 Electrochemically generation and accumulation of H_2O_2

After establishing a greater picture on the potential dependent selectivities via RRDE, in real applications, higher current densities are sought after. By using a gas diffusion setup (GDE), the oxygen reduction is not limited by the solubility of oxygen in the liquid electrolyte and oxygen can be fed directly in gaseous form to the catalyst's surface. The GDE setup allows the application of practical relevant current densities. The GDE cathode was fabricated by deposition of $Pd_{1\%}$/PCL6 onto a PW03 substrate. For comparison, PCL6/PW03 was studied. These experiments were accomplished with 150 mL in sulphate medium at pH 2.5, j = 33.3 mA cm^{-2} and 25 ºC. After 180 min of electrolysis, the maximum H_2O_2 concentrations varied between 1.33, 5.27 and 8.89 mM for PW03, PCL6/PW03 and $Pd_{1\%}$/PCL6/PW03, respectively (Fig. 4a). For PCL6 on PW03, the generation of H_2O_2 was increased by a factor of 3.9 compared to the bare PW03 substrate. For $Pd_{1\%}$/PCL6, the H_2O_2 generation was increased by a factor of 6.7 which is in line with RRDE results.

Fig. 4b shows a decrease in current efficiency (CE) over time. This effect is most pronounced for $Pd_{1\%}$/PCL6/PW03 with 36.9 % and 23.9 % CE after 20 and 180 min, respectively. For PCL6/PW03, the CE drops to 21.6 % and 14.1 %, respectively. H_2O_2 is not inert in solution and might be oxidized to hydroperoxyl radicals ($HO_2^{\bullet}$) (Eq. (6)) at the surface of the BDD anode, decreasing the overall CE (dos Santos et al., 2018b). This behavior has already been observed with other materials such as Pt and dimensional stable anodes (DSA) (Alcaide et al., 2020; Fajardo et al., 2019). $Pd_{1\%}$/PCL6/PW03 possesses the lowest energy consumption (EC) per kg_{H2O2} with 59.4 kWh $kg(H_2O_2)^{-1}$ (Fig. 4c), followed by PCL6/PW03 with 110.3 kWh $kg(H_2O_2)^{-1}$, and the bare PW03 substrate with 396.1 kWh $kg(H_2O_2)^{-1}$.

$$BDD + H_2O_2 \rightarrow BDD(HO_2\bullet) + H^+ + e^- \quad (6)$$

3.3.2 MetP degradation and energy consumption per order

Based on the promising results obtained with $Pd_{1\%}$/PCL6/PW03, its performance towards the degradation of organic pollutants was exemplarily tested on 0.50 mM MetP at pH 2.5, $j = 33.3$ mA cm^{-2} and 25 ºC by AO-H_2O_2, AO-H_2O_2/UVC, EF and PEP. After 180 min of treatment, AO-H_2O_2 leads to the lowest MetP degradation rate of 51.6 % as shown in Fig. 5a. Conversely, AO-H_2O_2/UV attains almost total degradation (95.8 %) under similar operating conditions.

The kinetic rate constants (k_1) fit well a pseudo-first-order kinetic model (c.f. Fig. 5b), with values of $6.90\text{x}10^{-5}$ s^{-1} ($R^2 = 0.991$) and $2.28\text{x}10^{-4}$ s^{-1} ($R^2 = 0.989$) for AO-H_2O_2 and AO-H_2O_2/UVC respectively. In the AO-H_2O_2 process, the greatest contribution to the MetP degradation is the physiosorbed •OH formed at the BDD anode surface from water electrolysis (Eq. (7)) (dos Santos et al., 2019; Garcia-Segura et al., 2018). The electrogeneration of H_2O_2 does not show any significant effect on the degradation of MetP, since H_2O_2 itself is considered a relatively weak oxidant ($E^o(H_2O_2/H_2O) = 1.76$ V_{SHE}) (dos Santos et al., 2018b), as well as $HO_2\bullet$. For AO-H_2O_2/UVC, the k_{app} increased by a factor of 3.3 that be related to additional generation of •OH radicals formed from H_2O_2 photodecomposition by UVC irradiation (Eq. (8)) (Moreira et al., 2017; Xu et al., 2019). MetP alone is relatively stable against UVC light (Fig. 5a) and only 12.7 % degrades after 180 min.

$$BDD + H_2O \rightarrow BDD(\bullet OH) + H^+ + e^- \quad (7)$$

$H_2O_2 + h\nu \rightarrow 2\ {\bullet}OH$ (8)

EF and PEF processes promote total degradation in less than 10 min (Fig. 5c). This rapid degradation is due to BDD(•OH) and the additional generation of high amounts of homogeneous •OH in the bulk by Fenton's reaction (Eq. (9)), that react rapidly with MetP. The necessary Fe^{2+} ion for Fenton's reaction can be regenerated by Eq. (10) and low catalyst concentrations can be used (Brillas, 2020; Garcia-Segura et al., 2014).

These processes should have an optimal ratio between H_2O_2 concentration generated and Fe^{2+} added. Therefore, various Fe^{2+} concentrations were tested (data not shown) in order to determine the ideal amount of this catalyst. We found that concentrations over 0.25 mM Fe^{2+}, excess of Fe^{2+} may scavenge •OH present in solution (Eq. (11)) (dos Santos et al., 2018c; Pérez et al., 2015). The obtained constant kinetics (k_1) were $5.52\text{x}10^{-3}\ s^{-1}$ ($R^2 = 0.997$) and $7.85\text{x}10^{-3}\ s^{-1}$ ($R^2 = 0.992$) for EF and PEF (c.f. Fig. 5d), respectively.

$Fe^{2+} + H_2O_2 + H^+ \rightarrow Fe^{3+} + {\bullet}OH + H_2O$ (9)

$Fe^{3+} + e^- \rightarrow Fe^{2+}$ (10)

$Fe^{2+} + {\bullet}OH \rightarrow Fe^{3+} + OH^-$ (11)

H_2O_2-based EAOPs can be compared in terms of the amount and costs related to the electrical energy per order required to reduce the concentration of the contaminant by one order of magnitude in a unit volume as shown in Eq. (12) (Garcia-Segura et al., 2020; Montenegro-Ayo et al., 2019):

$$E_{EO}(kWh\,m^{-3}order^{-1}) = \frac{6.39\times10^{-4}(P_{cell}+P_{lamp})}{V_s k_1} \quad (12)$$

Where 6.39×10^{-4} is a conversion factor (1 h/3600 s/0.4343), P_{cell} is the power of the electrochemical cell and P_{lamp} is the power of the lamp both in W, Vs is the solution volume in L and k_1 is the pseudo-first order rate constant in s^{-1}. The values of E_{EO} were 0.488 and 1.27 kWh m^{-3} order $^{-1}$ for EF and PEF, respectively. The E_{EO} for EF is by a factor of 2.6 lower compared to PEF, despite the fact that PEF has a 30% higher k_1 value compared to EF. From our results, the EF process seems the most economical viable process to degrade MetP in a real application.

3.3.3 MetP mineralization and by-products identification

As shown in Fig. 5e, the TOC removal was performed to evaluate the mineralization of 0.50 mM MetP (48 mg L^{-1} TOC). AO-H_2O_2 and AO-H_2O_2/UVC reached poor mineralization of 26.1% and 38.4%, respectively. The rate of TOC decrease is usually lower than the degradation rate due to the formation of by-products. Therefore, a longer treatment time is necessary to achieve high mineralization. In the EF process, during the first 90 min, the mineralization had a sharp decrease attaining a value of 45.9 %, remaining practically constant afterwards. This behavior may be because of the formation of Fe(III)-carboxylate complexes, formed during the degradation of MetP. These complexes are stable and highly resistant to the attack of •OH radicals (Antonin et al., 2015; Sopaj et al., 2016). For PEF, the process led to the best mineralization, with 90.1%. This can be explained by the photodecarboxylation of Fe(III)-carboxylate species ($Fe(OOCR)^{2+}$) via Eq. (13), along with the additional Fe^{2+} regeneration and •OH production from the photolysis of $FeOH^{2+}$ by Eq. (14) (Brillas, 2020; dos Santos et al., 2018b):

$$Fe(OOCR)^{2+} + h\nu \rightarrow Fe^{2+} + H_2O_2 + R\bullet \tag{13}$$

$$FeOH^{2+} + h\nu \rightarrow Fe^{2+} + \bullet OH \tag{14}$$

Fig. 5f reveals that the higher MCE values are related to the processes with higher oxidation capacity, following the order PEF > EF > AO-H_2O_2/UVC > AO-H_2O_2. During treatment, MCE remained constant for the AO-H_2O_2 and AO-H_2O_2/UVC processes as a consequence of their low mineralization power. However, MCE decreased for the others processes, in e.g. PEF to 38.7 %

and 21.5 % at 30 and 180 min, respectively. This is probably due to the decrease of organic matter with formation of recalcitrant by-products, as reported by other authors (Alcaide et al., 2020; Antonin et al., 2015; dos Santos et al., 2020).

Fig. 6 shows a proposed mineralization route for MetP. Aromatic intermediates and carboxylic acids were identified by GC-MS and ion exclusion HPLC, respectively. Table S5 summarizes the characteristics of by-products such as retention time and main fragmentation (m/z). The proposed mineralization route considered only the contribution of the heterogeneous and homogeneous $^{\bullet}OH$ formed on the surface of the BDD and Fenton's reactions, respectively. The degradation was initiated by the successive hydroxylation of **1** (MetP) that could yield the intermediates **2** (2,6-dihydroxy-methyl ester) and **3** (2, 5 -hydroxy-methylparaben). The attacks on the benzylic carbon atom of MetP bonded to the carbonyl group yielded **4** hydroquinone (Gmurek et al., 2015). The oxidation of hydroquinone causes the cleavage of the aromatic ring producing short-chain linear carboxylic acids. Intermediate **5** (oxalic acid) forms Fe(III)-oxalate complexes that can suffer photodecomposition under UVC, being then converted into CO_2 (Xu et al., 2019).

4. Conclusions

In summary, this work demonstrates that 1% of Pd NPs onto PCL6 is an active catalyst with an ~320 mV lower onset overpotential compared to bare PCL6. The selectivity towards H_2O_2 was close to 90% and its catalytic behavior was maintained after 5,000 degradation cycles between -0.2 and 0.5 $V_{Ag/AgCl}$. Pd1%/PCL6 was obtained in a single one-pot synthesis approach with high reproducibility that can potentially be scaled up. Fundamental studies were performed in an RRDE setup and extended to a more practical relevant GDE setup where oxygen gas can be directly fed to the catalysts surface. Exemplarily, the performance towards the degradation of 0.50 mM MetP by AO-H_2O_2 and AO-H_2O_2/UVC was tested revealing lower removal efficiencies compared to EF and PEF. The •OH radical produced in the bulk from Fenton's reaction demonstrated to be more reactive. For the Fenton-based processes, it was verified that the concentration of Fe^{2+} greatly affects the performance of the processes. The technology that led to the highest mineralization was PEF the 90.1 % operating with 21.5% of MCE. The mineralization route of MetP demonstrated the formation of three aromatic compounds and one short-chain carboxylic acid as final by-products.

ASSOCIATED CONTENT

Supporting Information. The supporting information contains experimental details, figures, equations, and tables concerning supplementary results, and references. This material is available free of charge via the Internet at:

ORCID

Guilherme V. Fortunato: 0000-0002-0768-4156
Matheus S. Kronka: 0000-0002-8518-2960
Alexsandro J. dos Santos: 0000-0002-5408-2238
Marc Ledendecker: 0000-0003-3740-401X
Marcos R.V. Lanza: 0000-0002-8285-7838

ACKNOWLEDGMENTS

The authors acknowledge the financial support provided by the following Brazilian funding agencies: Brazilian National Council for Scientific and Technological Development - CNPq (grant #465571/2014-0, #302874/2017-8 and #427452/2018-0), São Paulo Research Foundation (FAPESP – grants #2014/50945-4, #2017/23464-3 #2017/10118-0, #2019/04421-7 and #2019/20634-0), and the Coordenação de Aperfeiçoamento de Pessoal de Nível Superior (CAPES – Finance Code 001). ML acknowledges the Federal Ministry of Education and Research (BMBF) in the framework of NanoMatFutur (SynKat, FK: 03XP0265) for financial support. The authors thank the Laboratory of Structural Characterization (LCE/DEMa/UFSCar) for the general facilities.

References

Alcaide, F., Álvarez, G., Guelfi, D.R.V., Brillas, E., Sirés, I., 2020. A stable CoSP/MWCNTs air-diffusion cathode for the photoelectro-Fenton degradation of organic pollutants at pre-pilot scale. Chem. Eng. J. 379, 122417.

Antolini, E., 2012. Graphene as a new carbon support for low-temperature fuel cell catalysts. Appl. Catal. B: Environ. 123–124, 52–68.

Antonin, V.S., Garcia-Segura, S., Santos, M.C., Brillas, E., 2015. Degradation of Evans Blue diazo dye by electrochemical processes based on Fenton's reaction chemistry. J. Electroanal. Chem. 747, 1–11.

Assumpção, M.H.M.T., De Souza, R.F.B., Rascio, D.C., Silva, J.C.M., Calegaro, M.L., Gaubeur, I., Paixão, T.R.L.C., Hammer, P., Lanza, M.R.V., Santos, M.C., 2011. A comparative study of the electrogeneration of hydrogen peroxide using Vulcan and Printex carbon supports. Carbon N. Y. 49, 2842–2851.

Barros, W.R.P., Wei, Q., Zhang, G., Sun, S., Lanza, M.R.V., Tavares, A.C., 2015. Oxygen reduction to hydrogen peroxide on Fe3O4 nanoparticles supported on Printex carbon and Graphene. Electrochim. Acta 162, 263–270.

Boone, C. V., Maia, G., 2019. Lowering metal loadings onto Pt–Pd–Cu/graphene nanoribbon nanocomposites affects electrode collection efficiency and oxygen reduction reaction performance. Electrochim. Acta 303, 192–203.

Boone, C. V., Maia, G., 2017. Pt–Pd and Pt–Pd–(Cu or Fe or Co)/graphene nanoribbon nanocomposites as efficient catalysts toward the oxygen reduction reaction. Electrochim. Acta 247, 19–29.

Brillas, E., 2020. A review on the photoelectro-Fenton process as efficient electrochemical advanced oxidation for wastewater remediation. Treatment with UV light, sunlight, and coupling with conventional and other photo-assisted advanced technologies. Chemosphere 250, 126198.

Brillas, E., Martínez-Huitle, C.A., 2015. Decontamination of wastewaters containing synthetic organic dyes by electrochemical methods. An updated review. Appl. Catal. B: Environ. 166–167, 603–643.

Campos-Martin, J.M., Blanco-Brieva, G., Fierro, J.L.G., 2006. Hydrogen peroxide synthesis: An outlook beyond the anthraquinone process. Angew. Chemie - Int. Ed. 45, 6962–6984.

Carneiro, J.F., Paulo, M.J., Siaj, M., Tavares, A.C., Lanza, M.R. V, 2017. Zirconia on Reduced Graphene Oxide Sheets: Synergistic Catalyst with High Selectivity for H2O2 Electrogeneration. ChemElectroChem 4, 508–513.

Carneiro, J.F., Silva, F.L., Martins, A.S., Dias, R.M.P., Titato, G.M., Santos-Neto, Á.J., Bertazzoli, R., Lanza, M.R.V., 2018. Simultaneous degradation of hexazinone and diuron using ZrO2-nanostructured gas diffusion electrode. Chem. Eng. J. 351, 650–659.

Choi, C.H., Kwon, H.C., Yook, S., Shin, H., Kim, H., Choi, M., 2014. Hydrogen peroxide synthesis via enhanced two-electron oxygen reduction pathway on carbon-coated pt surface. J. Phys. Chem. C 118, 30063–30070.

Cordeiro-Junior, P.J.M., Gonçalves, R., Guaraldo, T.T., da Silva Paiva, R., Pereira, E.C., Lanza, M.R. de V., 2020. Oxygen reduction reaction: Semi-empirical quantum mechanical and electrochemical study of Printex L6 carbon black. Carbon N. Y. 156, 1–9.

Daems, N., Sheng, X., Vankelecom, I.F.J., Pescarmona, P.P., 2014. Metal-free doped carbon materials as electrocatalysts for the oxygen reduction reaction. J. Mater. Chem. A 2, 4085–4110.

Damjanovic, A., Genshaw, M.A., Bockris, J.O., 1967. The Role of hydrogen peroxide in oxygen reduction at platinum in H2SO4 solution. J. Electrochem. Soc. 114, 466–472.

Dionisio, D., Santos, L.H.E., Rodrigo, M.A., Motheo, A.J., 2020. Electro-oxidation of methyl paraben on DSA®-Cl2: UV irradiation, mechanistic aspects and energy consumption. Electrochim. Acta 338, 135901.

Dirany, A., Sirés, I., Oturan, N., Özcan, A., Oturan, M.A., 2012. Electrochemical treatment of the antibiotic sulfachloropyridazine: kinetics, reaction pathways, and toxicity evolution. Environ. Sci. Technol. 46, 4074–4082.

Dominguez, C.M., Oturan, N., Romero, A., Santos, A., Oturan, M.A., 2018. Removal of lindane wastes by advanced electrochemical oxidation. Chemosphere 202, 400–409.

dos Santos, A.J., Costa, E.C.T. de A., da Silva, D.R., Garcia-Segura, S., Martínez-Huitle, C.A., 2018a. Electrochemical advanced oxidation processes as decentralized water treatment technologies to remediate domestic washing machine effluents. Environ. Sci. Pollut. Res. 25, 7002–7011.

dos Santos, A.J., Garcia-Segura, S., Dosta, S., Cano, I.G., Martínez-Huitle, C.A., Brillas, E., 2019. A ceramic electrode of ZrO2-Y2O3 for the generation of oxidant species in anodic oxidation. Assessment of the treatment of Acid Blue 29 dye in sulfate and chloride media. Sep. Purif. Technol. 228, 115747.

dos Santos, A.J., Martínez-Huitle, C.A., Sirés, I., Brillas, E., 2018b. Use of Pt and boron-doped diamond anodes in the electrochemical advanced oxidation of Ponceau SS diazo dye in acidic sulfate medium. ChemElectroChem 5, 685–693.

dos Santos, A.J., Sirés, I., Alves, A.P.M., Martínez-Huitle, C.A., Brillas, E., 2020. Vermiculite as heterogeneous catalyst in electrochemical Fenton-based processes: Application to the oxidation of Ponceau SS dye. Chemosphere 240, 124838.

dos Santos, A.J., Sirés, I., Alves, A.P.M., Martínez-Huitle, C.A., Brillas, E., de Lima, M.D., da Silva, D.R., Garcia-Segura, S., Martínez-Huitle, C.A., 2016. Influence of the water hardness on the performance of electro-Fenton approach: Decolorization and mineralization of Eriochrome Black T. Electrochim. Acta 208, 156–163.

dos Santos, A.J., Sirés, I., Martínez-Huitle, C.A., Brillas, E., 2018c. Total mineralization of mixtures of Tartrazine, Ponceau SS and Direct Blue 71 azo dyes by solar photoelectro-Fenton in pre-pilot plant. Chemosphere 210, 1137–1144.

Edwards, J.K., Freakley, S.J., Lewis, R.J., Pritchard, J.C., Hutchings, G.J., 2015. Advances in the direct synthesis of hydrogen peroxide from hydrogen and oxygen. Catal. Today 248, 3–9.

Fabbri, E., Taylor, S., Rabis, A., Levecque, P., Conrad, O., Kötz, R., Schmidt, T.J., 2014. The effect of platinum nanoparticle distribution on oxygen electroreduction activity and selectivity. ChemCatChem 6, 1410-1418. https://doi.org/10.1002/cctc.201300987

Fajardo, A.S., dos Santos, A.J., de Araújo Costa, E.C.T., da Silva, D.R., Martínez-Huitle, C.A., 2019. Effect of anodic materials on solar photoelectro-Fenton process using a diazo dye as a model contaminant. Chemosphere 225, 880–889.

Fdez-Sanromán, A., Acevedo-García, V., Pazos, M., Sanromán, M.Á., Rosales, E., 2020. Iron-doped cathodes for electro-Fenton implementation: Application for pymetrozine degradation. Electrochim. Acta 338, 135768.

Fellinger, T.P., Hasché, F., Strasser, P., Antonietti, M., 2012. Mesoporous nitrogen-doped carbon for the electrocatalytic synthesis of hydrogen peroxide. J. Am. Chem. Soc. 134, 4072–4075.

Fortunato, G. V., de Lima, F., Maia, G., 2016. Oxygen-reduction reaction strongly electrocatalyzed by Pt electrodeposited onto graphene or graphene nanoribbons. J. Power

Sources 302, 247–258.

Fortunato, G. V., Pizzutilo, E., Mingers, A.M., Kasian, O., Cherevko, S., Cardoso, E.S.F., Mayrhofer, K.J.J., Maia, G., Ledendecker, M., 2018. Impact of palladium loading and interparticle distance on the selectivity for the oxygen reduction reaction toward hydrogen peroxide. J. Phys. Chem. C 122, 15878–15885.

Ganiyu, S.O., Oturan, N., Raffy, S., Cretin, M., Esmilaire, R., van Hullebusch, E., Esposito, G., Oturan, M.A., 2016. Sub-stoichiometric titanium oxide (Ti4O7) as a suitable ceramic anode for electrooxidation of organic pollutants: A case study of kinetics, mineralization and toxicity assessment of amoxicillin. Water Res. 106, 171–182.

Ganiyu, S.O., Vieira dos Santos, E., Tossi de Araújo Costa, E.C., Martínez-Huitle, C.A., 2018. Electrochemical advanced oxidation processes (EAOPs) as alternative treatment techniques for carwash wastewater reclamation. Chemosphere 211, 998–1006.

Garcia-Segura, S., Cavalcanti, E.B., Brillas, E., 2014. Mineralization of the antibiotic chloramphenicol by solar photoelectro-Fenton. Appl. Catal. B: Environ. 144, 588–598. https://doi.org/10.1016/j.apcatb.2013.07.071

Garcia-Segura, S., Nienhauser, A.B., Fajardo, A.S., Bansal, R., Coonrod, C.L., Fortner, J.D., Marcos-Hernández, M., Rogers, T., Villagran, D., Wong, M.S., Westerhoff, P., 2020. Disparities between experimental and environmental conditions: Research steps toward making electrochemical water treatment a reality. Curr. Opin. Electrochem. 22, 9–16.

Garcia-Segura, S., Ocon, J.D., Chong, M.N., 2018. Electrochemical oxidation remediation of real wastewater effluents — A review. Process Saf. Environ. Prot. 113, 48–67.

Gmurek, M., Rossi, A.F., Martins, R.C., Quinta-Ferreira, R.M., Ledakowicz, S., 2015. Photodegradation of single and mixture of parabens – Kinetic, by-products identification and cost-efficiency analysis. Chem. Eng. J. 276, 303–314.

Han, L., Sun, Y., Li, S., Cheng, C., Halbig, C.E., Feicht, P., Hübner, J.L., Strasser, P., Eigler, S., 2019. In-plane carbon lattice-defect regulating electrochemical oxygen reduction to hydrogen peroxide production over nitrogen-doped graphene. ACS Catal. 9, 1283–1288.

Inaba, M., Yamada, H., Tokunaga, J., Tasaka, A., 2004. Effect of agglomeration of Pt/C catalyst on hydrogen peroxide formation. Electrochem. Solid-State Lett. 7, A474.

Jiang, H., Gu, J., Zheng, X., Liu, M., Qiu, X., Wang, L., Li, W., Chen, Z., Ji, X., Li, J., 2019. Defect-rich and ultrathin N doped carbon nanosheets as advanced trifunctional metal-free electrocatalysts for the ORR, OER and HER. Energy Environ. Sci. 12, 322–333.

Jiang, Y., Ni, P., Chen, C., Lu, Y., Yang, P., Kong, B., Fisher, A., Wang, X., 2018. Selective electrochemical H2O2 production through two-electron oxygen electrochemistry. Adv. Energy Mater. 8, 1801909.

Jukk, K., Alexeyeva, N., Sarapuu, A., Ritslaid, P., Kozlova, J., Sammelselg, V., Tammeveski, K., 2013. Electroreduction of oxygen on sputter-deposited Pd nanolayers on multi-walled carbon nanotubes. Int. J. Hydrogen Energy 38, 3614–3620.

Kabir, S., Serov, A., Zadick, A., Artyushkova, K., Atanassov, P., 2016. Palladium nanoparticles supported on three-dimensional graphene nanosheets: superior cathode electrocatalysts. ChemElectroChem 3, 1655–1666.

Kim, H.W., Park, H., Roh, J.S., Shin, J.E., Lee, T.H., Zhang, L., Cho, Y.H., Yoon, H.W., Bukas, V.J., Guo, J., Park, H.B., Han, T.H., McCloskey, B.D., 2019. Carbon defect characterization of nitrogen-doped reduced graphene oxide electrocatalysts for the two-electron oxygen reduction reaction. Chem. Mater. 31, 3967–3973.

Lima, V.B., Goulart, L.A., Rocha, R.S., Steter, J.R., Lanza, M.R.V., 2020. Degradation of antibiotic ciprofloxacin by different AOP systems using electrochemically generated hydrogen peroxide. Chemosphere 247, 125807.

Lobyntseva, E., Kallio, T., Alexeyeva, N., Tammeveski, K., Kontturi, K., 2007. Electrochemical synthesis of hydrogen peroxide: Rotating disk electrode and fuel cell studies. Electrochim. Acta 52, 7262–7269.

Lu, Y., Sehrish, A., Manzoor, R., Dong, K., Jiang, Y., 2019. Recent progress on electrochemical production of hydrogen peroxide. Chem. Reports 1, 81–101.

Luo, Y., Alonso-Vante, N., 2015. The effect of support on advanced Pt-based cathodes towards the oxygen reduction reaction. State of the Art. Electrochim. Acta 179, 108–118.

Ma, J., Habrioux, A., Morais, C., Lewera, A., Vogel, W., Verde-Gómez, Y., Ramos-Sanchez, G., Balbuena, P.B., Alonso-Vante, N., 2013. Spectroelectrochemical probing of the strong interaction between platinum nanoparticles and graphitic domains of carbon. ACS Catal. 3, 1940–1950.

Marković, N.M., Gasteiger, H.A., Grgur, B.N., Ross, P.N., 1999. Oxygen reduction reaction on Pt(111): effects of bromide. J. Electroanal. Chem. 467, 157–163.

Melchionna, M., Fornasiero, P., Prato, M., 2019. The rise of hydrogen peroxide as the main product by metal-free catalysis in oxygen reductions. Adv. Mater. 31, 1802920.

Mittermeier, T., Weiß, A., Gasteiger, H.A., Hasché, F., 2017. Monometallic palladium for oxygen reduction in PEM fuel cells: particle-size effect, reaction mechanism, and voltage cycling stability. J. Electrochem. Soc. 164, F1081–F1089.

Montenegro-Ayo, R., Morales-Gomero, J.C., Alarcon, H., Cotillas, S., Westerhoff, P., Garcia-Segura, S., 2019. Scaling up photoelectrocatalytic reactors: A TiO2 nanotube-coated disc compound reactor effectively degrades acetaminophen. Water 11, 2522.

Moreira, F.C., Boaventura, R.A.R., Brillas, E., Vilar, V.J.P., 2017. Electrochemical advanced oxidation processes: A review on their application to synthetic and real wastewaters. Appl. Catal. B: Environ. 202, 217–261.

Nakamura, K.C., Guimarães, L.S., Magdalena, A.G., Angelo, A.C.D., De Andrade, A.R., Garcia-Segura, S., Pipi, A.R.F., 2019. Electrochemically-driven mineralization of Reactive Blue 4 cotton dye: On the role of in situ generated oxidants. J. Electroanal. Chem. 840, 415–422.

Nesselberger, M., Roefzaad, M., Fayçal Hamou, R., Ulrich Biedermann, P., Schweinberger, F.F., Kunz, S., Schloegl, K., Wiberg, G.K.H.H., Ashton, S., Heiz, U., Mayrhofer, K.J.J., Arenz, M., 2013. The effect of particle proximity on the oxygen reduction rate of size-selected platinum clusters. Nat. Mater. 12, 919–924.

Paz, E.C., Aveiro, L.R., Pinheiro, V.S., Souza, F.M., Lima, V.B., Silva, F.L., Hammer, P., Lanza, M.R.V., Santos, M.C., 2018. Evaluation of H2O2 electrogeneration and decolorization of Orange II azo dye using tungsten oxide nanoparticle-modified carbon. Appl. Catal. B: Environ. 232, 436–445.

Pérez, T., Garcia-Segura, S., El-Ghenymy, A., Nava, J.L., Brillas, E., 2015. Solar photoelectro-Fenton degradation of the antibiotic metronidazole using a flow plant with a Pt/air-diffusion cell and a CPC photoreactor. Electrochim. Acta 165, 173–181.

Pesterfield, L., 2009. The 100 most important chemical compounds: a reference guide (by Richard L. Myers). J. Chem. Educ. 86, 1182.

Ren, G., Zhou, M., Zhang, Q., Xu, X., Li, Y., Su, P., 2020. A novel stacked flow-through electro-Fenton reactor as decentralized system for the simultaneous removal of pollutants (COD, NH3-N and TP) and disinfection from domestic sewage containing chloride ions. Chem. Eng. J. 387, 124037.

Rosa Barbosa, M.P., Lima, N.S., de Matos, D.B., Alves Felisardo, R.J., Santos, G.N., Salazar-Banda, G.R., Cavalcanti, E.B., 2018. Degradation of pesticide mixture by electro-Fenton in filter-press reactor. J. Water Process Eng. 25, 222–235.

Saha, J., Dandapat, A., De, G., 2011. Transformation of Pd → PdH0.7 nanoparticles inside mesoporous Zr-modified SiO2 films in ambient conditions. J. Mater. Chem. 21, 11482.

Schmidt, T.J., Paulus, U.A., Gasteiger, H.A., Behm, R.J., 2001. The oxygen reduction reaction on a Pt/carbon fuel cell catalyst in the presence of chloride anions. J. Electroanal. Chem. 508, 41–47.

Schneider, A., Colmenares, L., Seidel, Y.E., Jusys, Z., Wickman, B., Kasemo, B., Behm, R.J., 2008. Transport effects in the oxygen reduction reaction on nanostructured, planar glassy carbon supported Pt/GC model electrodes. Phys. Chem. Chem. Phys. 10, 1931.

Scofield, J.H., 1976. Hartree-Slater subshell photoionization cross-sections at 1254 and 1487 eV. J. Electron Spectros. Relat. Phenomena 8, 129–137.

Siahrostami, S., Verdaguer-Casadevall, A., Karamad, M., Deiana, D., Malacrida, P., Wickman, B., Escudero-Escribano, M., Paoli, E.A., Frydendal, R., Hansen, T.W., Chorkendorff, I., Stephens, I.E.L., Rossmeisl, J., 2013. Enabling direct H2O2 production through rational electrocatalyst design. Nat. Mater. 12, 1137–1143.

Sopaj, F., Oturan, N., Pinson, J., Podvorica, F., Oturan, M.A., 2016. Effect of the anode materials on the efficiency of the electro-Fenton process for the mineralization of the antibiotic sulfamethazine. Appl. Catal. B: Environ. 199, 331–341.

Steter, J.R., Brillas, E., Sirés, I., 2016. On the selection of the anode material for the electrochemical removal of methylparaben from different aqueous media. Electrochim. Acta 222, 1464–1474.

Su, J., Ge, R., Dong, Y., Hao, F., Chen, L., 2018. Recent progress in single-atom electrocatalysts: concept, synthesis, and applications in clean energy conversion. J. Mater. Chem. A 6, 14025–14042.

Taylor, S., Fabbri, E., Levecque, P., Schmidt, T.J., Conrad, O., 2016. The effect of platinum loading and surface morphology on oxygen reduction activity. Electrocatalysis 7, 287–296.

Venarusso, L.B., Bettini, J., Maia, G., 2016. Catalysts for oxygen reduction reaction based on nanocrystals of a Pt or Pt–Pd alloy shell supported on a Au core. J. Solid State Electrochem. 20, 1753–1764.

Venarusso, L.B., Boone, C. V, Bettini, J., Maia, G., 2018. Carbon-supported metal nanodendrites as efficient, stable catalysts for the oxygen reduction reaction. J. Mater. Chem. A 6, 1714–1726.

Verdaguer-casadevall, A., Deiana, D., Karamad, M., Siahrostami, S., Malacrida, P., Hansen, T.W., Rossmeisl, J., Chorkendorff, I., Stephens, I.E.L., Chorkendor, I., Stephens, I.E.L., 2014. Trends in the electrochemical synthesis of H2O2 : enhancing activity and selectivity by electrocatalytic site engineering. Nano Lett. 14, 1603–1608.

Vukmirovic, M.B., Bliznakov, S.T., Sasaki, K., Wang, J.X., Adzic, R.R., 2011. Electrodeposition of metals in catalyst synthesis: the case of platinum monolayer electrocatalysts. Interface Mag. 20, 33–40.

Wu, K.-H., Wang, D.-W., Zong, X., Zhang, B., Liu, Y., Gentle, I.R., Su, D.-S., 2017. Functions in cooperation for enhanced oxygen reduction reaction: the independent roles of oxygen and nitrogen sites in metal-free nanocarbon and their functional synergy. J. Mater. Chem. A 5, 3239–3248.

Xu, A., Brillas, E., Han, W., Wang, L., Sirés, I., 2019. On the positive effect of UVC light during the removal of benzothiazoles by photoelectro-Fenton with UVA light. Appl. Catal. B: Environ. 259, 118127.

Yan, W.M., Chu, H. Sen, Liu, Y.L., Chen, F., Jang, J.H., 2011. Effects of chlorides on the performance of proton exchange membrane fuel cells. Int. J. Hydrogen Energy 36, 5435–5441.

Zhang, H., Lv, K., Fang, B., Forster, M.C., Dervişoğlu, R., Andreas, L.B., Zhang, K., Chen, S., 2018. Crucial role for oxygen functional groups in the oxygen reduction reaction electrocatalytic activity of nitrogen-doped carbons. Electrochim. Acta 292, 942–950.

Zhang, Yinqiao, Zuo, S., Zhang, Ying, Ren, G., Pan, Y., Zhang, Q., Zhou, M., 2019. Simultaneous removal of tetracycline and disinfection by a flow-through electro-peroxone process for reclamation from municipal secondary effluent. J. Hazard. Mater. 368, 771–777.

Figures captions.

Fig. 1. Representative (a and c) virtual high-angle angular dark field (images reconstructed from electron diffraction patterns), (b and d) bright-field STEM, and (e) HR-TEM images of $Pd_{1\%}$ /PCL6. (f) Size distribution histograms and interparticle distance (*ipd*) for $Pd_{1\%}$/PCL6.

Fig. 2. Physico-chemical characterization of PCL6 and $Pd_{1\%}$/PCL6 catalysts. (a) Thermogravimetric responses. (b) XRD patterns. (c) Survey XPS spectra for PCL6 and $Pd_{1\%}$/PCL6. (d) Narrow scan XPS spectrum for Pd 3d regions of $Pd_{1\%}$ /PCL6 catalysts.

Fig. 3. (a, b) Cyclic voltammograms obtained in N_2 and O_2-sat 0.1 mol L^{-1} K_2SO_4 at pH 2.5 for GC electrodes modified with PCL6 and $Pd_{1\%}$ /PCL6 (scan rate: 50 mV s^{-1}; scans started at 1.0 $V_{Ag/AgCl}$). (c) Linear sweep voltammetry in an RRDE configuration scanning the potential at 5 mV s^{-1} and 900 rpm in O_2-sat 0.1 mol L^{-1} K_2SO_4 at pH 2.5 (scans started at -0.9 or -0.2 $V_{Ag/AgCl}$). (d) $S_{H_2O_2}$ during the ORR at varying potentials (obtained from the corresponding RRDE data). (e, f) Linear sweep RDE results scanning the potential at 5 mV s^{-1} recorded in O_2-sat 0.1 mol L^{-1} K_2SO_4 at pH 2.5 solution at various rotation rates. Insets: corresponding K-L plots.

Fig. 4. Influence of different cathodes on (a) accumulated H_2O_2 concentration vs time (b) current efficiency and (c) energy consumed per kg H_2O_2 using 150 mL of 50 mM Na_2SO_4 solution at pH 2.5 and 25 °C, using (●) PW03, (■) PCL6/PW03 and (▼) $Pd_{1\%}$/PCL6/PW03/gas diffusion.

Fig. 5. Effect of different H_2O_2 based EAOPs (▲)AO-H_2O_2, (▼)AO-H_2O_2/UV, (■) EF and (●) PEF on the treatment of 0.50 mM of MetP solutions at pH 2.5 and j = 33.3 mA cm^{-2}. (a) and (b) MetP degradation over time; (c) and (d) Pseudo-first order kinetics; (e) TOC removal over time; (f) mineralization efficiency over time. (■) only UVC light.

Fig. 6. Reaction sequence for MetP mineralization by the PEF process using a $Pd_{1\%}$/PCL6/PW03 gas diffusion cathode and a BDD anode.

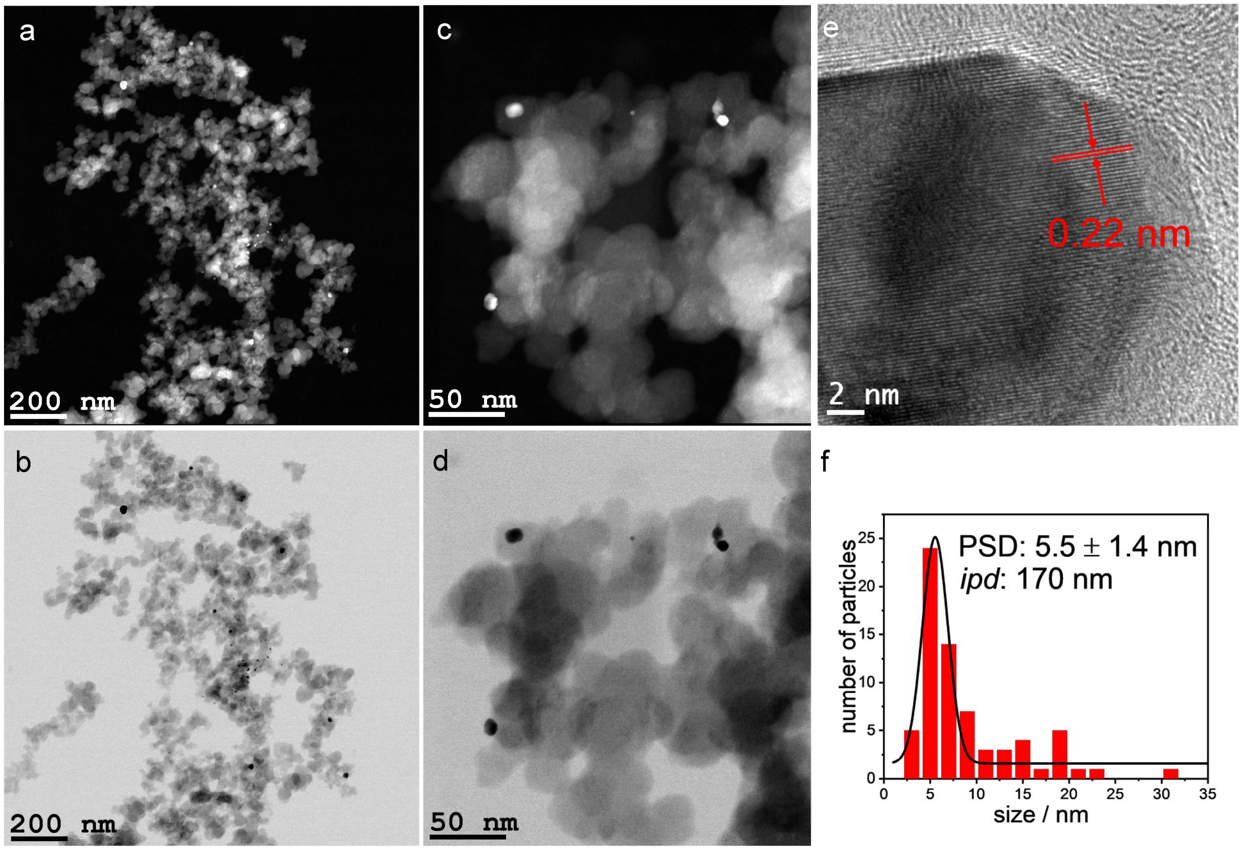
a
200 nm
b
200 nm
c
50 nm
d
50 nm
e
0.22 nm
2 nm
f
PSD: 5.5 ± 1.4 nm
ipd: 170 nm
number of particles
size / nm
0
5
10
15
20
25
30
35

Fig. 1.

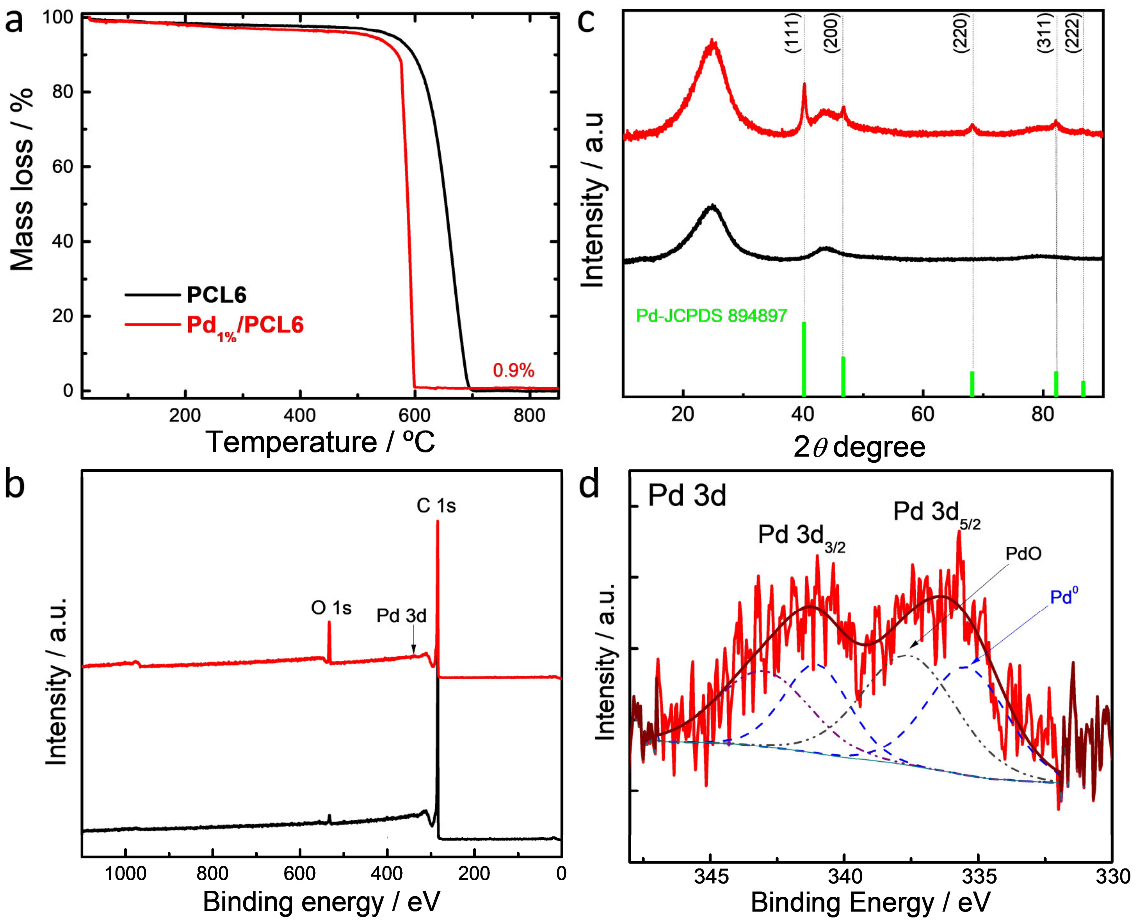
a
Mass loss / %
100
80
60
40
20
0
200
400
600
800
Temperature / ºC
PCL6
Pd1%/PCL6
0.9%
b
Intensity / a.u.
C 1s
O 1s
Pd 3d
1000
800
600
400
200
0
Binding energy / eV
c
Intensity / a.u
(111)
(200)
(220)
(311)
(222)
Pd-JCPDS 894897
20
40
60
80
2θ degree
d
Pd 3d
Pd 3d3/2
Pd 3d5/2
PdO
Pd0
Intensity / a.u.
345
340
335
330
Binding Energy / eV

Fig. 2.

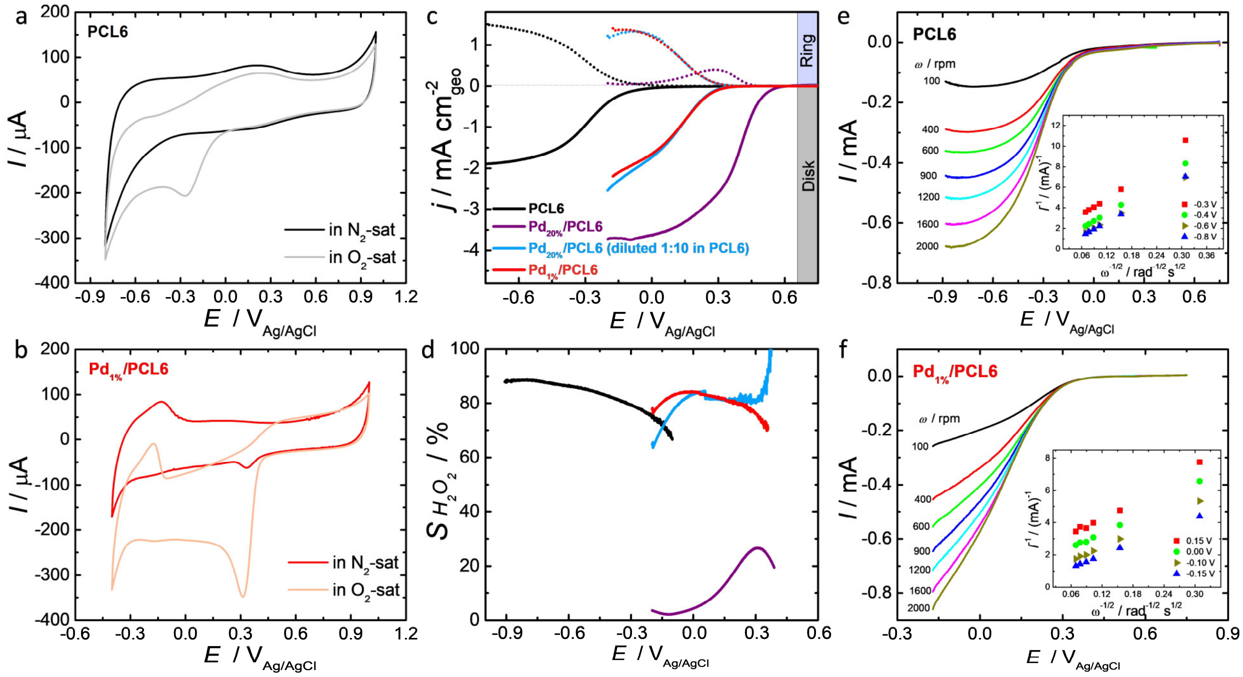
a
PCL6
in N2-sat
in O2-sat
I / μA
E / VAg/AgCl
b
Pd1%/PCL6
in N2-sat
in O2-sat
I / μA
E / VAg/AgCl
c
j / mA cm-2geo
Ring
Disk
PCL6
Pd20%/PCL6
Pd20%/PCL6 (diluted 1:10 in PCL6)
Pd1%/PCL6
E / VAg/AgCl
d
SH2O2 / %
E / VAg/AgCl
e
PCL6
ω / rpm
100
400
600
900
1200
1600
2000
I / mA
E / VAg/AgCl
I-1 / (mA)-1
ω-1/2 / rad-1/2 s1/2
-0.3 V
-0.4 V
-0.6 V
-0.8 V
f
Pd1%/PCL6
ω / rpm
100
400
600
900
1200
1600
2000
I / mA
E / VAg/AgCl
I-1 / (mA)-1
ω-1/2 / rad-1/2 s1/2
0.15 V
0.00 V
-0.10 V
-0.15 V

Fig. 3.

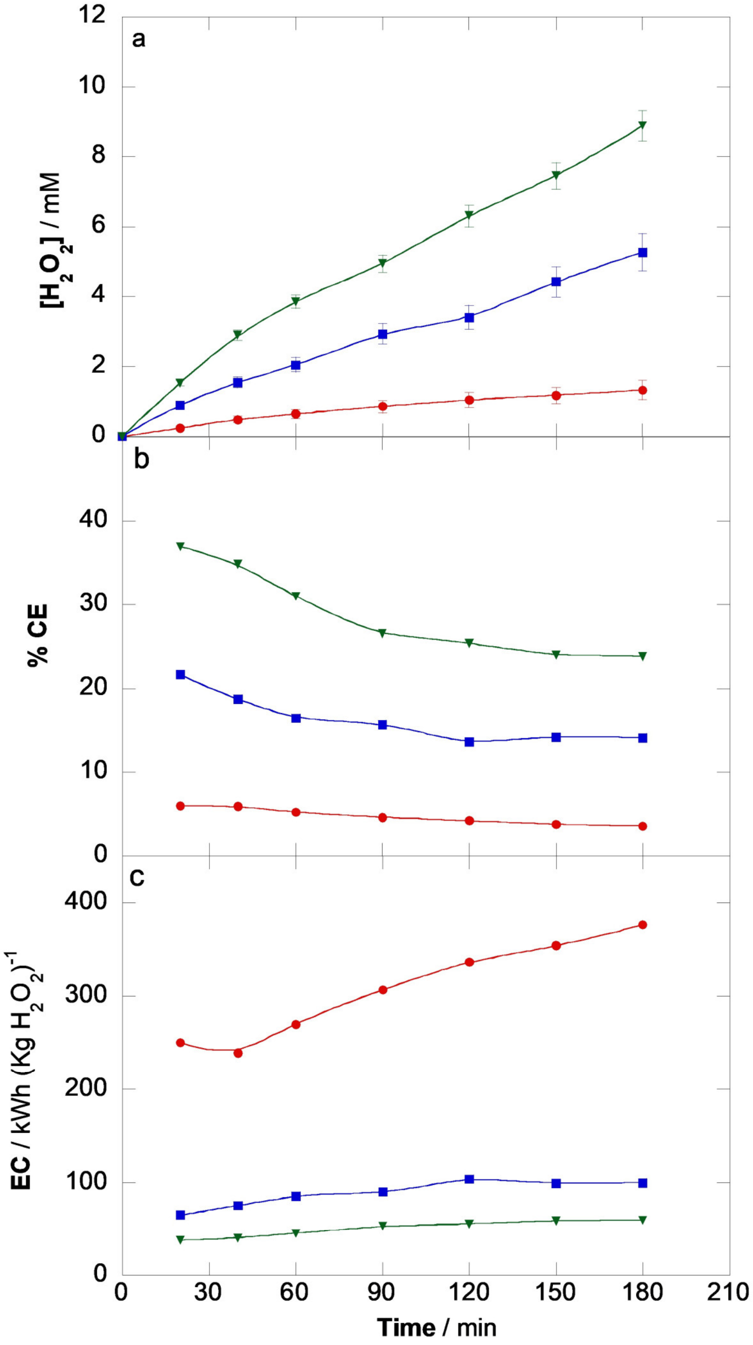

a
[H_2O_2] / mM
0
2
4
6
8
10
12
b
% CE
0
10
20
30
40
c
EC / kWh (Kg H_2O_2)$^{-1}$
0
100
200
300
400
0
30
60
90
120
150
180
210
Time / min

Fig. 4.

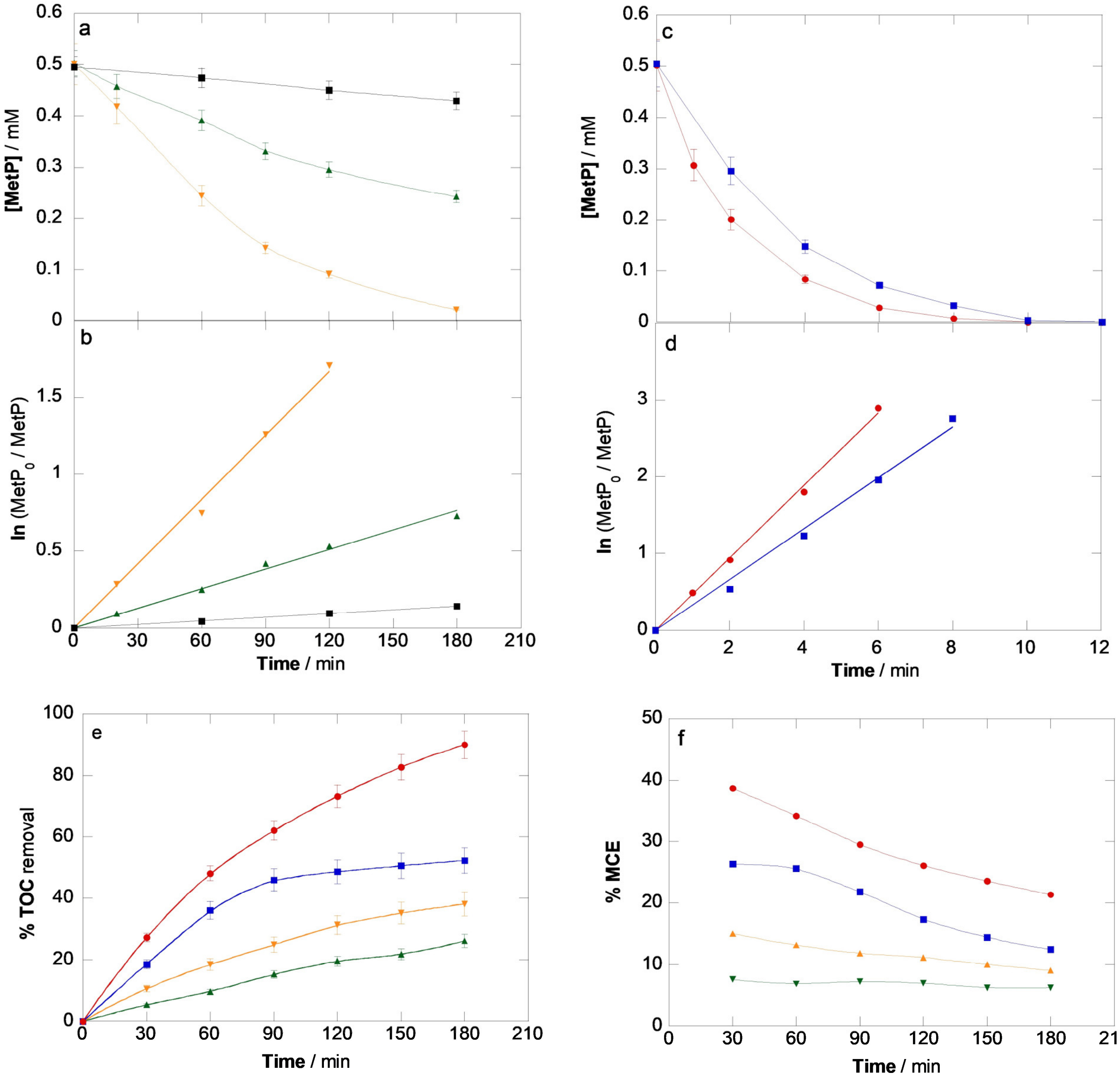
a
b
c
d
e
f
[MetP] / mM
ln (MetP$_0$ / MetP)
% TOC removal
% MCE
Time / min
0
0.1
0.2
0.3
0.4
0.5
0.6
0.5
1
1.5
2
3
20
40
60
80
100
10
30
50
0
30
60
90
120
150
180
210
2
4
6
8
10
12

Fig. 5.

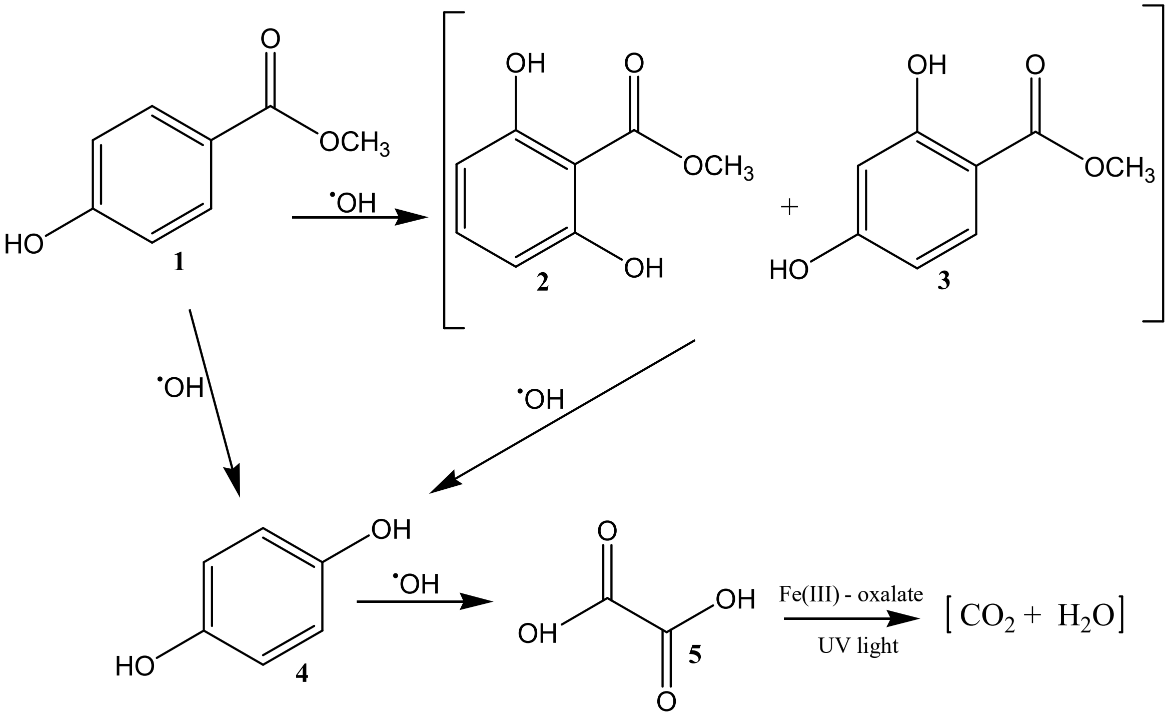

O
OCH3
HO
1
•OH
OH
O
OCH3
OH
2
+
OH
O
OCH3
HO
3
•OH
•OH
OH
HO
4
•OH
O
OH
OH
5
O
Fe(III) - oxalate
UV light
[CO2 + H2O]

Fig. 6.